Research Article Vol. 13, No. 12 / 1 Dec 2023 / Optical Materials Express 3641
Optical Materials EXPRESS

Predictive visualisation of high repetition rate femtosecond machining of silica using deep learning

BEN MILLS,* JAMES A. GRANT-JACOB, AND MICHALIS N. ZERVAS

Optoelectronics Research Centre, University of Southampton, UK
*bm602@orc.soton.ac.uk

Abstract: Whilst femtosecond laser machining can enable extremely high-resolution fabrication, it is a highly nonlinear process that is challenging to model when starting from basic principles and a theoretical understanding. Deep learning offers the potential for modelling complex systems directly from experimental data, and hence is a complementary alternative to traditional modelling approaches. In this work, deep learning is applied to the predictive visualisation of femtosecond laser machining of lines in a silica substrate, in a specific experimental regime where nanofoam is fabricated. The neural networks used for this task are shown to consider both the laser power and the amount of debris on the sample before machining, when predicting the appearance of the line after machining. This predictive capability provides clear evidence of the potential for deep learning to become an important tool in the understanding and optimisation of laser machining, and indeed, other complex physical phenomena.

1. Introduction

Femtosecond laser machining [1–3] offers the potential for extremely high resolution sample fabrication [4,5], as the heat affected zone is minimised [6,7]. However, when incident on a target material, femtosecond laser pulses can result in an extremely wide range of complex phenomena, including nonlinear absorption and the generation of plasma [8]. These highly nonlinear atom-photon dynamics mean that modelling femtosecond laser machining by starting from a theoretical understanding is generally too computational challenging to provide accurate and practically useful information. Therefore, in practice, a trial-and-error approach to fabrication optimisation is typically applied to femtosecond laser machining, where the laser user will manually and systemically optimise all experimental parameters (such as laser power, spot size, and scanning speed) to fabricate a sample that most closely approximates the desired sample appearance.

Deep learning [9,10], which generally involves the application of deep neural networks, offers the prospect for the modelling and optimisation of extremely complex systems directly from associated data, and hence offers an interesting and complementary alternative to the traditional approach of modelling a system from a theoretical understanding. In recent years, deep learning has started to be applied to the field of optimising, modelling and predictive visualisation of laser machining [11–16], with overviews of this rapidly developing field provided by a series of review articles [17,18].

In this work, the femtosecond laser focus is scanned over the sample using a set of specific experimental conditions that results in the production of nanofoam, which is understood to be a complex volume of nanowires that are fabricated at the interaction point during laser machining [19–22]. Previous work has proposed that the fabrication mechanism of nanofoam is based on

#505746 https://doi.org/10.1364/OME.505746
Journal © 2023 Received 11 Sep 2023; revised 8 Nov 2023; accepted 11 Nov 2023; published 29 Nov 2023

Optical Materials EXPRESS

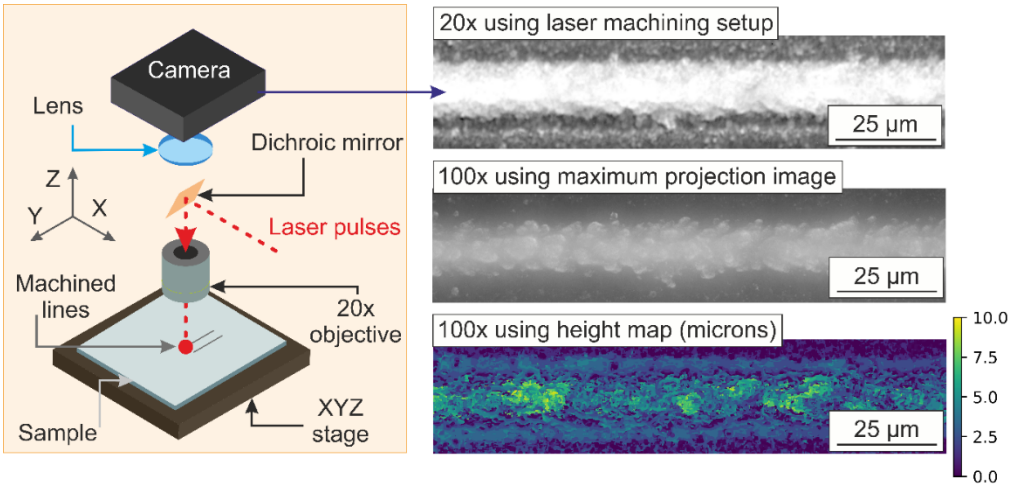

Fig. 1. Experimental setup, and an image of a laser-machined line at a laser power of 100% recorded on the 20× imaging system on the laser machining setup, along with a maximum projection image and height map recorded using a separate 100× optical microscope.

the ejection of debris from the laser plasma, where the super-heated debris particles leave a vapour trail that is condensed into the nanowires that are visible after machining [23]. Given the very complex and nonlinear nature of this specific regime of femtosecond laser machining, and the potential for nanofoam to be used in an array of advanced applications, such as energy storage [24,25] and biomedical sciences [26,27], there is a clear advantage in developing practical techniques that can be used to predict the appearance of the laser machined sample under different experimental conditions, and this is a key motivation for this work. As presented here, the neural networks indicate that both the laser power and the amount of debris on the sample before machining influences the appearance of the sample after machining, hence demonstrating the potential for using data-driven modelling of experimental data for parameter optimisation and scientific discovery.

2. Experimental methods and data collection

A Light Conversion Pharos SP laser was used to generate pulses with a duration of 190 fs with a maximum energy of 30 μJ, repetition rate of 200 kHz, and central wavelength of 1030 nm. These pulses were focused onto the sample surface (silica glass slide, brand = Corning) using a 20× Nikon objective (TU Plan ELWD, 0.40 NA, 19 mm working distance), achieving a maximum laser fluence on the sample of approximately 10 mJcm^{-2}. The laser focus was scanned over the sample at 0.2 mm/s. The experimental setup included a camera (Basler a2A5320-23ucPRO, 5328 × 3040 pixels) to capture images of the sample surface, as depicted in Fig. 1. The sample was positioned on a motorized XYZ translation stage (Thorlabs) for automated movement. The camera, translation stages and laser were controlled using Python for automated data collection. The figure shows a single example of a region of a laser machined line, at a laser power of 100% (where 100% corresponds to the maximum laser pulse energy of 30 μJ), imaged using the camera on the laser machining setup. This line was subsequently imaged on a separate microscope (Nikon, 100x SLMPlan, Basler acA3088-57uc 3088 × 2064 pixels) and an image was recorded in steps of 1 μm along the focal direction. This allowed a 3D volume of images to be recorded, which was then used to produce a maximum projection image through taking the highest pixel value along the focal direction, and a height map of the sample through analysis of Fourier components in the images. For the height map, the non-machined areas of the sample are set to a

Optical Materials EXPRESS

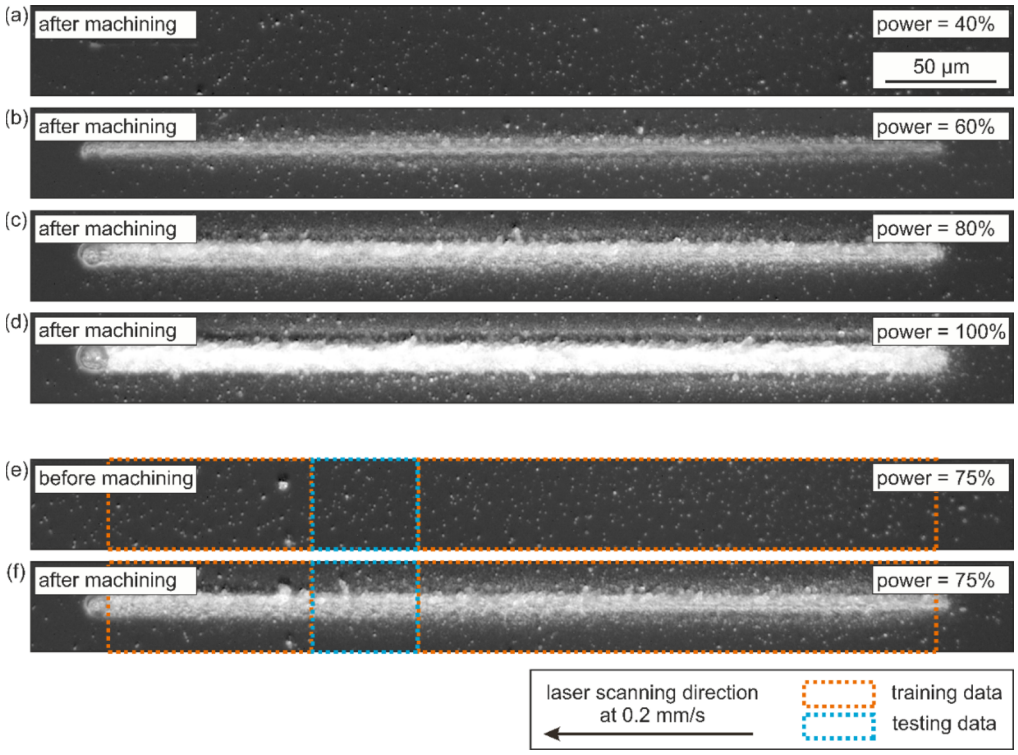

Fig. 2. Example experimental data for (a)-(d) lines machined with different laser powers, and (e)-(f) a comparison of the appearance of the sample before and after machining, and the regions of the images selected for training and testing of the neural networks.

height of 0 µm, and hence the figure shows that the sample has increased in height up to 10 µm, owing to the fabrication process.

For each laser machined line, the sample was moved to the mid-way point (i.e., half way between the proposed start and end of the line) and a camera image recorded, then the sample was moved to the start of the line and the laser power was set to the required value and the laser pulses turned on. A request was then sent to the stages to move to the end of the line, and when this movement was complete the laser pulses were turned off. The stages were then moved back to the middle of the line and a camera image recorded. Therefore, for each line, an image of the sample before and after laser machining was recorded. Due to small positional errors (of order 5 µm per 400 µm machined line) caused by the backlash of the translation stages, the before and after images were slightly offset and needed to be repositioned to ensure the pairs of before and after images corresponded to the same region of the sample. This was achieved using Fourier transforms and the cross-correlation function on the before and after images, where the region that had been machined was masked as this region would be different for the two images. Both images were transformed into the frequency domain using the Fourier transform, resulting in two complex-valued frequency domain representations. The cross-correlation operation was then applied by multiplying the Fourier transform of one image by the complex conjugate of the Fourier transform of the other image. The inverse Fourier transform was then applied to this result to obtain the cross-correlation map, which had a peak corresponding to the best alignment position in the spatial domain. Using this method, the images were overlapped to an accuracy better than one image pixel. All lines in the training data were machined with a fixed power (between 30% and 100%) and were 400 µm long, as this corresponded to the field of view of the

Optical Materials EXPRESS

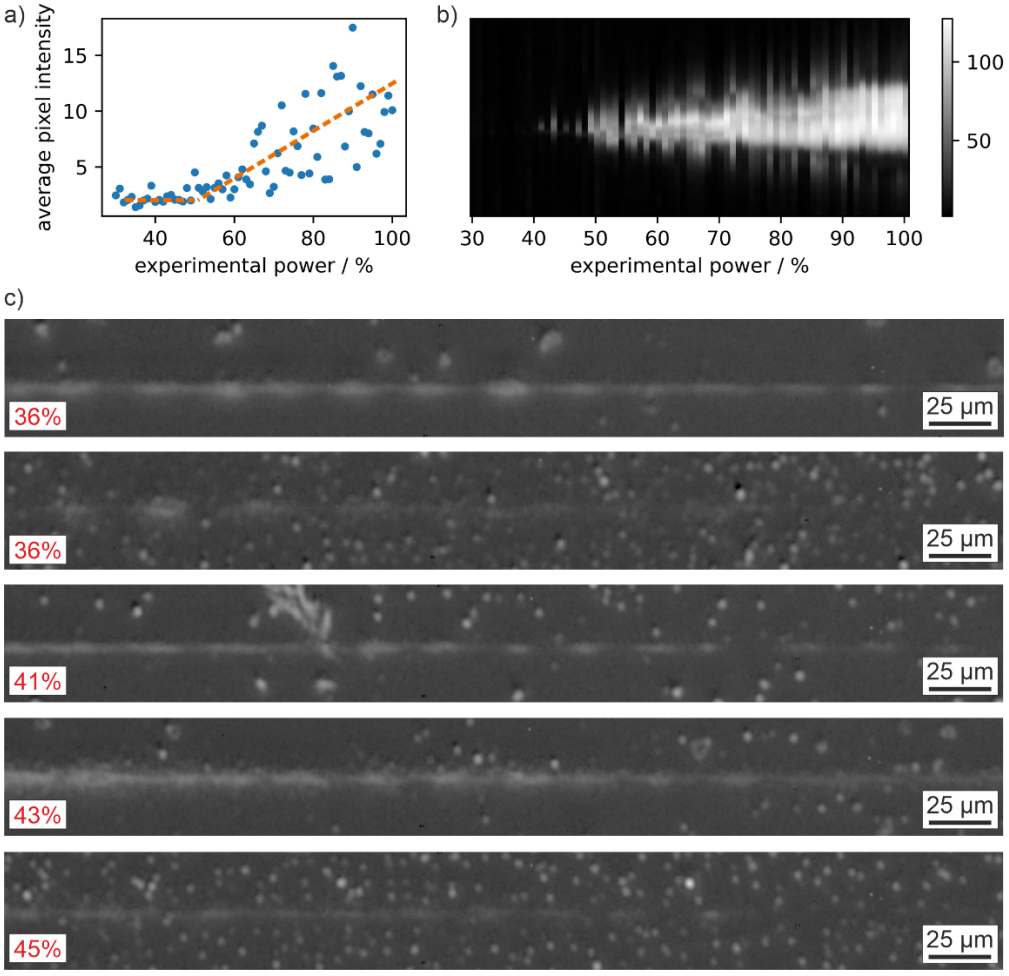

Fig. 3. Analysis of experimental data and the produced debris, showing a) average pixel values (corresponding approximately to the amount of produced debris) and b) 2D slices across the machined lines for different laser powers, and c) five examples of lines machined at laser powers close to the machining threshold.

camera and hence ensured that the entire length of each line was recorded on a single camera image. Additional lines, where the power was varied randomly during the machining of the line were also recorded, but were not included in the training data. The scan speed of 0.2 mm/s was fixed for the entire experiment. The length of each line, as recorded on the camera, was approximately 3000 camera pixels, meaning that each cropped 256×256 pixel image (the image size used for the neural networks) was approximately 34 µm wide.

A total of 368 lines were machined, with examples of experimentally recorded images shown in Fig. 2, where all lines in the figure correspond to a fixed laser power. Parts (a)-(d) show the results of machining at 40% to 100% power, and (e)-(f) show a comparison of the appearance of the sample before and after machining for a power of 75%, with orange and blue dotted regions indicating the approach for separation the experimental data into the training and testing categories for the application of neural networks. The start and end of the lines were removed from the training and testing data and, due to a slight instability under certain conditions, the data region selected for testing was chosen slightly to the left of the centre of the line. The laser

Optical Materials EXPRESS

power values for each line were randomly chosen (from a uniform distribution between 30% and 100%) to ensure a varied level of laser-produced debris on the sample, as subsequent lines had a high amount of debris before machining if the previous line had power of 100%, or a low amount debris if the previous line had a power value lower than 40%. Adjacent lines were separated by 50 microns, and a manual refocus step was completed after machining after every seventh line.

Figure 3 provides evidence that the laser power has a nonlinear effect on the degree of machining of the sample and the resultant production of debris. Part a) presents the average pixel intensity in the experimental after images when the laser machined regions were masked, and hence approximately indicates the relationship between laser power and amount of produced debris, and b) shows examples of 2D slices across the machined lines that indicate the average change in width of the lines. This analysis indicates that the laser machining threshold was around 40% of the maximum laser power. As shown in c), which presents five examples of experimental images of lines machined at lower powers, machining with a laser power close to this threshold generally resulted in lines with an intermittent appearance. This is attributed to small deviations in laser power and the presence of surface debris causing some regions of the lines to not be machined.

3. Prediction of laser power used for machining

As shown in Fig. 4(a), a neural network was applied to experimental images of the sample after machining (cropped to 256×256 pixels) to predict the laser power used for machining. Under the experimental conditions used in this work, the presence of debris before machining has been shown to have a significant impact on the appearance of the sample after machining. The motivation for attempting to identify the laser power from images of machined lines was to therefore identify whether a neural network could learn to consider the amount of debris present on the sample when predicting the laser power used to machine the line. As shown by the accuracy metric for all test data in (b), and the images provided in (c)-(f), the neural network was indeed successful in predicting the power from the experimentally recorded images. Parts (g)-(h) and (i)-(j) present examples of experimental images corresponding to the same laser power but with different levels of debris, hence resulting in considerably different appearances of the laser machined line. The fact that the neural network was able to correctly predict the power in the cases of (g)-(h) and (i)-(j) indicates that the network appears to be considering both the appearance of the line and the surrounding debris. The ability of the network to predict the laser power when no line had been machined is attributed to the width of the horizontal line across the image that corresponds to the removal of debris by the low power laser pulses.

The power identification task was completed using a convolutional neural network with a single regression output, where the input image was a single channel experimental microscope image cropped to 256×256 image pixels, and the output was the predicted power percentage value. The network consisted of 18 layers, which reduced the spatial dimensions of the input image down to a $1 \times 1 \times 1$ output. The training parameters consisted of a minibatch size of 2, an initial learn rate of 0.0001, ADAM optimizer, RMSE loss function, learn rate drop factor of 0.1 and period of 50, and 10 epochs of training. Images were augmented by random cropping through a random positional variation of 64 camera pixels in the vertical direction, and any position along the horizontal direction. The network was trained using MATLAB on a Microsoft Windows 10 computer workstation with 3× NVIDIA A4050s (20 GB each), with an Intel Xeon Gold 5222 CPU @3.80 GHz and 3.79 GHz, and 192 GB RAM.

Optical Materials EXPRESS

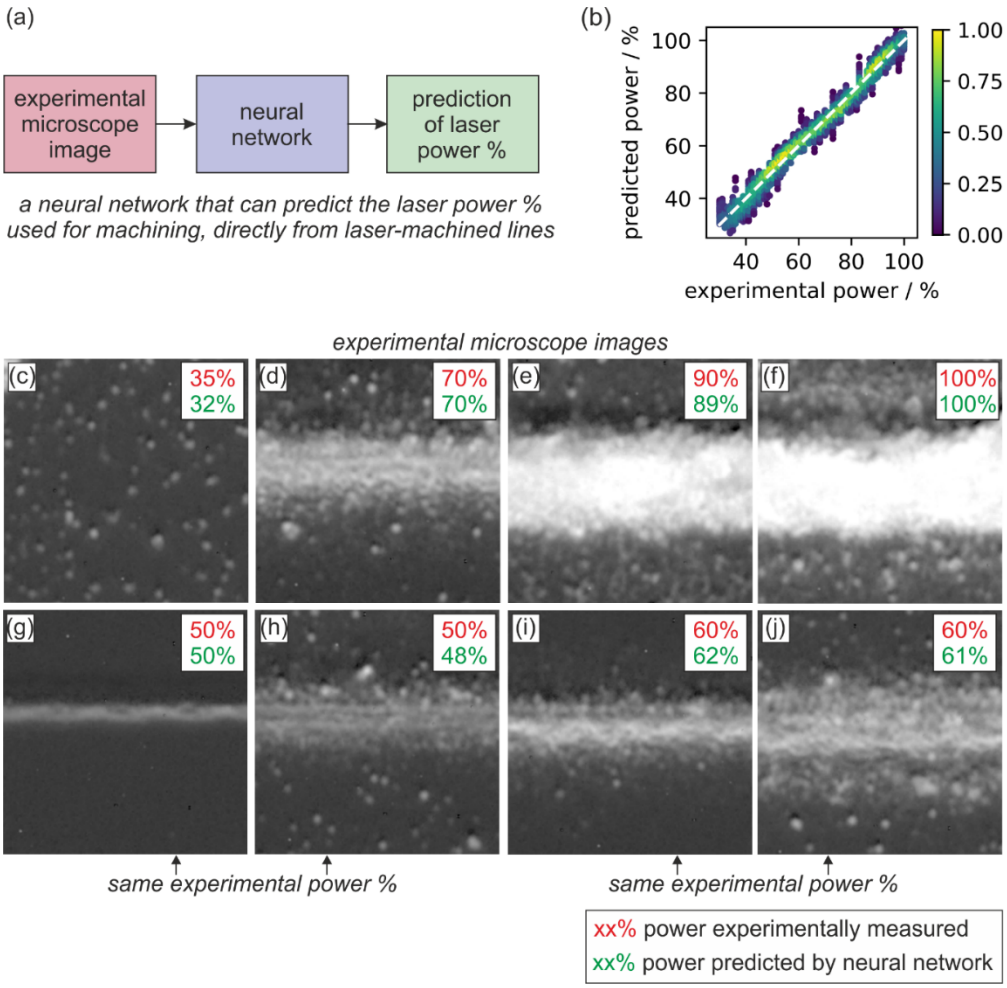

Fig. 4. Showing (a) neural network concept, (b) predictive accuracy for all test data, and (c)-(j) examples of experimental images and associated predictions by the neural network. Note that (g)-(h) and (i)-(j) are the same experimental power but result in a considerably different appearance, due to the presence of debris before machining (where the amount of debris present before machining can be identified by the amount of debris at the top and bottom of the images).

4. Prediction of sample appearance after machining for fixed power

Figure 5 presents the capability of a neural network that was trained to predict the appearance of the sample after machining, when provided with both the appearance of the sample before machining and the laser power, with (a) showing the concept of the network. Figure 5(b) provides an accuracy metric, through the comparison of the experimental images and the predicted images of the sample after machining for all test data, with the Y-axis of the figure showing the difference in the averaged white level of the pixels in the images (which varied from 0 to 255). In general, good agreement was achieved, with reduced accuracy for higher laser powers.

Figure 5(c) shows a set of experimental images before machining ("before"), the images predicted by the neural network ("predicted"), and experimental images after machining ("real"), for a range of laser powers. Sets of data are presented for (left) lower and (right) higher amounts

Optical Materials EXPRESS

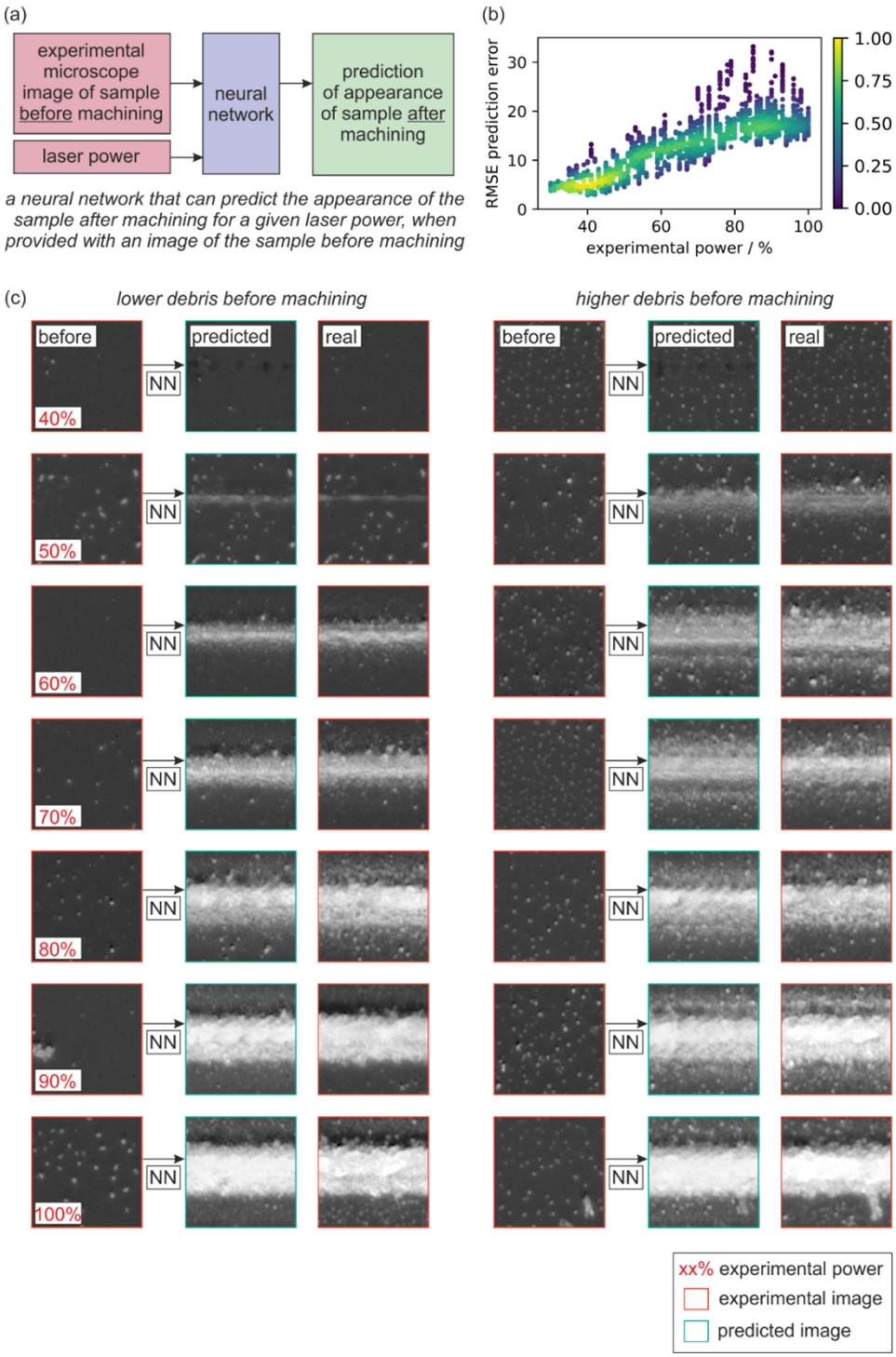

Fig. 5. Showing a) the concept of the predictive neural network, b) accuracy of the predictive network at different laser powers for all test data, c) examples of images for 'before machining', 'network prediction' and 'after machining', for different power values. Showing (left column) less and (right column) more initial debris, indicating that the predictive neural network considers both the power and the appearance of the sample before machining, when making a prediction.

Optical Materials EXPRESS

of debris before machining. It is clear that the predictions from the neural network take into account both the amount of debris and the laser power, with the effect most noticeable for power values in the range 50% to 70%, which is a result similarly observed for the convolutional neural network (Fig. 4) that was trained to predict laser power. The predicted images in Fig. 5(c) generally show comparable line widths, along with the appearance of the machined structures. As expected, at the top and bottom of the images, where there is no laser machining taking place, the debris in the predicted image is identical in position and appearance to the debris in the experimental image of the sample before machining. However, there are some imperfections in the neural network predictions for 40% power, where a set of black marks appear in the middle of the predicted image.

The results in Fig. 5(c)) for the predictions at 40% power show black marks where one might expect the appearance of a laser machined structure. Whilst it is not possible to directly interrogate the network to identify the cause, this effect is likely to be related to characteristics in the training data around the threshold value. As shown in Fig. 3(c)), when the laser machining process operates at power levels around the threshold, it exhibits an inconsistent outcome, resulting in machined lines with an intermittent appearance. It is therefore plausible that the black marks appearing in the generated outputs at threshold powers exist as the network has learned and internalized the intermittent property of laser-machined lines in the vicinity of the power threshold. Further evidence for this hypothesis is that the black marks do not appear in generated images for power values greater than 50%.

The neural network used for predictive visualisation of the sample after machining was a conditional generative adversarial network that used the "pix2pix" architecture [28] for transforming experimental images of the sample before machining into predicted images of the sample after machining. The input and output images were three-channel, where all pixels in the red channel (for both the input and output images) had a pixel value that encoded the laser power. This pixel value was calculated using the laser power minus 30, all multiplied by 3, to give a range of pixel values between 0 and 210, hence fitting within the 8-bit unsigned integer maximum value of 255. The network generator comprised of a U-Net structure that firstly reduced the size of the input image before upscaling back to the original input dimensions, along with a discriminator that was used to judge whether the generated images were realistic in appearance. The network was trained using a minibatch size of 2, a generator and discriminator learn rate of 0.002, an L1-to-GAN loss ratio of 100:1, an ADAM optimizer, and was trained for 5 epochs. Data was augmented through random cropping of images down to 256×256 pixels along the horizontal direction. The network was trained using MATLAB on a Microsoft Windows 10 computer workstation, with an AMD Ryzen Threadripper PRO 3995WX 64-Cores 2.70 GHz CPU, 512 GB of RAM and $4 \times$ NVIDIA A5000 GPUs (24 GB memory each).

5. Prediction of sample appearance after machining for varying power

The neural network used for predicting the appearance of lines was limited to 256×256 pixels, corresponding to an experimental distance of approximately 34×34 µm. However, as shown in Fig. 6, the output of multiple predictions can be concatenated to predict the appearance of extended regions of laser machined lines. This concatenation approach also allows predictive visualisation for a machined line where the laser power varies along its length. To demonstrate this, Fig. 6 presents a line machined with a varying power, with measured power values shown in (a). The laser power was changed during machining of the line through direct control of the laser attenuator, and the power values shown in Fig. 6(a) were confirmed through the use of the convolutional neural network presented in Fig. 4.

In Fig. 6(a), the red crosses show the average power for each 256×256 region, and hence corresponded to the power used for the predictive neural network for each predicted image. The experimental image before machining is shown in (b), which was used, with the average laser

Optical Materials EXPRESS

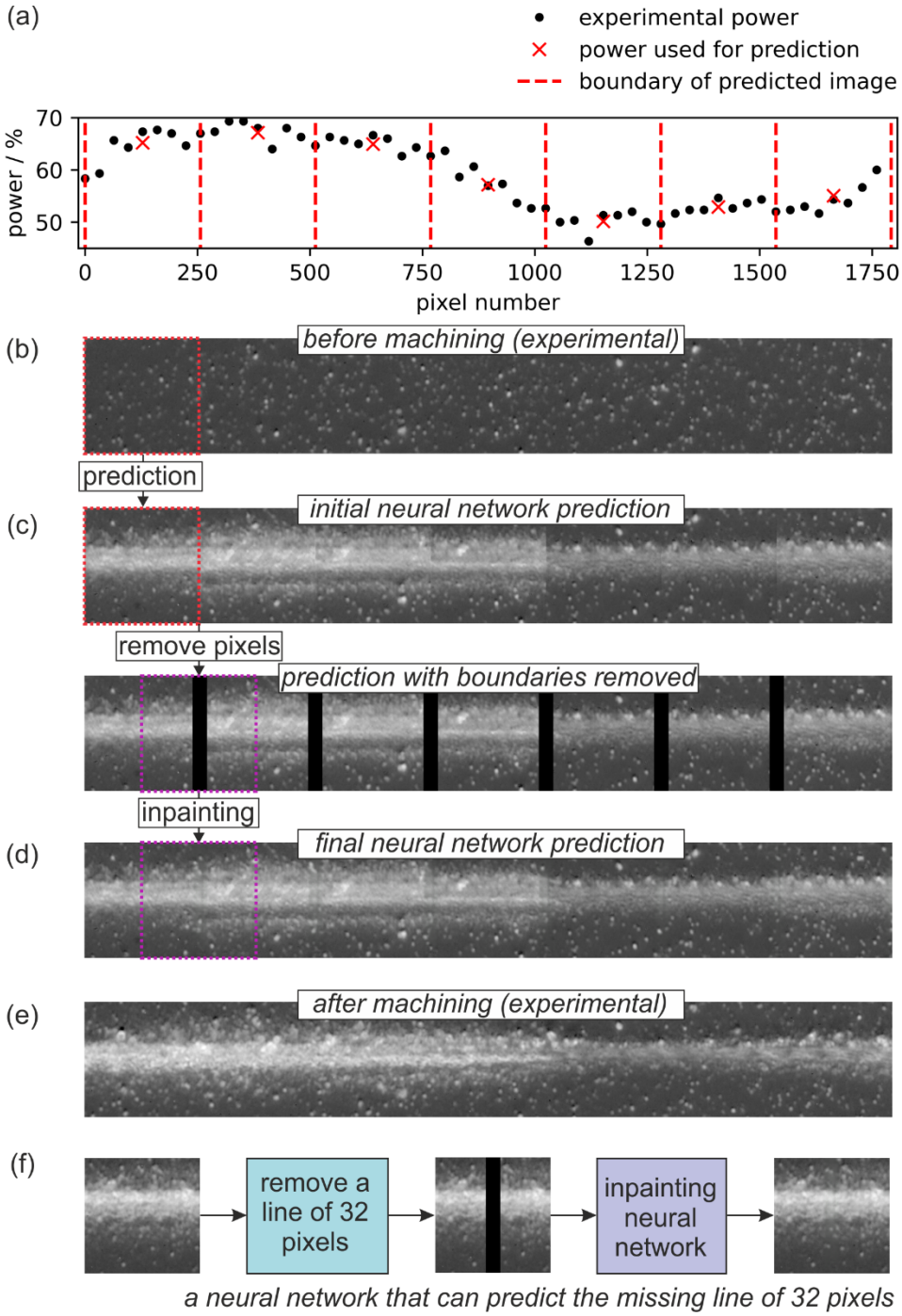

Fig. 6. Showing (a) the experimental power (black dots) and the average power used for the neural network (red crosses), (b) the experimental image of the sample before machining, (c) the network prediction of the sample after machining, also using an inpainting approach, and (d) the final network prediction, which can be compared to the equivalent experimental result in (e). Part (f) shows the concept of the inpainting network.

Optical Materials EXPRESS

power, as the input image to the network. As each 256×256 predicted image was generated independently, there existed a noticeable interface between each set of adjacent images when they were concatenated. This effect was removed through the masking of a width of 32 image pixels at the interface between each set of images, followed by the application of an inpainting neural network that generated a new set of images pixels that suitably merged the two adjacent image together. The final neural network prediction (i.e., after the image inpainting step) is shown in (d), and this prediction can be compared to the equivalent experimental result in (e). Generally, good agreement is shown between (d) and (e), and the predicted line is visibly associated with a varying laser power. However, it is visually apparent that the predicted line is formed of individual images, particularly around the regions where the laser power is changing more rapidly. The degree of predicted image discretisation could be reduced in future by using smaller sections of predicted images, for example using predicted images of 128 pixels wide (rather than the presented images of 256 pixels wide).

The concept of the inpainting network is shown in (f), which shows how a neural network was implemented to generate the masked pixels in a 256×256 image, by being trained on all experimental images in the training data set. As the same inpainting network was trained to identify the masked pixels for all laser powers, the network could be applied to predict the masked image pixels between predicted images of different laser powers, and hence be used to assist in the prediction of extended lines with varying powers. Figure 6(f) shows an example of the masking of an experimental image at a power of 75%, along with the associated predicted image. In general, the outputs from the inpainting network were found to be realistic in terms of both the distribution of generated debris and the width and appearance of the inpainted line. However, on closer inspection, the inpainted regions have a slightly higher white level than the surrounding image pixels. The inpainting neural network had an identical architecture to the predictive visualisation network, and was trained under the same parameters and using the same computer hardware. The training data for the inpainting network was augmented through random cropping of the lines in the horizontal direction.

A significant challenge in the application of deep learning for modelling laser machining is the collection of the experimental data required for training, as each data item generally requires a physical laser machining process. Scaling up to large amounts of experimental data therefore requires carefully designed automation procedures. In this work, a 20× microscope objective was used to focus the femtosecond laser pulses to the desired spot size on the sample. To collect data during machining, the same objective was therefore also used to image the sample, hence restricting the resolution of the experimental images collected for this work. Similarly, due to the available computational hardware, the size of the image that could be predicted by a neural network was limited to 256×256 pixels. The consequence here was that the experimental data was cropped to regions of 256×256 pixels, where the scaling was such that the machined line for 100% laser power was approximately half the width of the image. Whilst this approach was appropriate for the results presented here, future work could benefit from considerably higher resolution images, for example scanning electron microscopy images of the sample. Although automated data collection of scanning electron images would require a substantial upgrade in automation capability, such an approach would certainly provide a significant amount of additional data for future deep learning implementations. Recent work has also shown the applicability of using images of the plasma [29] generated during laser machining, and there are likely other modalities that will also be useful for understanding and modelling femtosecond laser machining using a data-driven paradigm.

The image-to-image neural network used for this work for predicting the appearance of the sample after machining was designed to be a general-purpose image transformation tool, and as such included a U-Net generator with skip connections, and made use of both an adversarial and L1 loss. The large number of convolutional filters in the network ensured that a wide range

Optical Materials EXPRESS

of image features could be learnt and generated by the network. Therefore, the network used in this work was not designed specifically for the prediction task presented here, and it might be that optimisation of the network architecture would provide some minor improvements in the predictive accuracy. However, in practice, the most effective way to improve the predictive accuracy would almost certainly be to collect more experimental data.

6. Conclusions

In conclusion, we have demonstrated the application of deep learning for the prediction of the appearance of a silica substrate after femtosecond laser machining of lines, when the laser power and an experimental image of the sample before machining is known. The neural network used for predicting the sample appears to consider both the laser power and the degree of debris on the sample before machining, and this result provides quantitative evidence that, under specific regimes of experimental conditions, debris on the sample before machining is strongly correlated with the amount of nanofoam that is produced. The same approach, with the addition of an inpainting network, was used to predict the appearance of laser machined lines with varying powers. The results presented here show an implementation of data-driven visualisation of highly nonlinear femtosecond laser machining, and hence provides evidence for the potential use of deep learning for modelling and understanding complex physical phenomena.

Funding. Engineering and Physical Sciences Research Council (EP/P027644/1, EP/T026197/1, EP/W028786/1).

Disclosures. The authors declare no conflicts of interest.

Data availability. Data underlying the results presented in this paper are available in Ref. [30].

References

1. R. R. Gattass and E. Mazur, "Femtosecond laser micromachining in transparent materials," Nat. Photonics **2**(4), 219–225 (2008).
2. K. T. Ahmmed, C. Grambow, and A.-M. Kietzig, "Fabrication of micro/nano structures on metals by femtosecond laser micromachining," Micromachines **5**(4), 1219–1253 (2014).
3. B. Ali, I. V. Litvinyuk, and M. Rybachuk, "Femtosecond laser micromachining of diamond: Current research status, applications and challenges," Carbon **179**, 209–226 (2021).
4. D. J. Heath, J. A. Grant-Jacob, R. W. Eason, *et al.*, "Single-pulse ablation of multi-depth structures via spatially filtered binary intensity masks," Appl. Opt. **57**(8), 1904–1909 (2018).
5. R. Sahin, E. Simsek, and S. Akturk, "Nanoscale patterning of graphene through femtosecond laser ablation," Appl. Phys. Lett. **104**(5), 053118 (2014).
6. M. S. Amer, M. El-Ashry, L. R. Dosser, *et al.*, "Femtosecond versus nanosecond laser machining: comparison of induced stresses and structural changes in silicon wafers," Appl. Surf. Sci. **242**(1-2), 162–167 (2005).
7. R. Le Harzic, N. Huot, E. Audouard, *et al.*, "Comparison of heat-affected zones due to nanosecond and femtosecond laser pulses using transmission electronic microscopy," Appl. Phys. Lett. **80**(21), 3886–3888 (2002).
8. F. Huang, J. Si, T. Chen, *et al.*, "Temporal-spatial dynamics of electronic plasma in femtosecond laser induced damage," Opt. Express **29**(10), 14658–14667 (2021).
9. A. Krizhevsky, I. Sutskever, and G. E. Hinton, "Imagenet classification with deep convolutional neural networks," Commun. ACM **60**(6), 84–90 (2017).
10. 1N Rusk, "Deep learning," Nat. Methods **13**(1), 35 (2016).
11. B. Mills, D. J. Heath, J. A. Grant-Jacob, *et al.*, "Predictive capabilities for laser machining via a neural network," Opt. Express **26**(13), 17245–17253 (2018).
12. K. Bamoto, H. Sakurai, S. Tani, *et al.*, "Autonomous parameter optimization for femtosecond laser micro-drilling," Opt. Express **30**(1), 243–254 (2022).
13. K. Shimahara, S. Tani, H. Sakurai, *et al.*, "A deep learning-based predictive simulator for the optimization of ultrashort pulse laser drilling," Communications Engineering **2**(1), 1 (2023).
14. S. Tani and Y. Kobayashi, "Ultrafast laser ablation simulator using deep neural networks," Sci. Rep. **12**(1), 5837 (2022).
15. M. D. McDonnell, D. Arnaldo, E. Pelletier, *et al.*, "Machine learning for multi-dimensional optimisation and predictive visualisation of laser machining," Journal of Intelligent Manufacturing **32**(5), 1471–1483 (2021).
16. K. Rani, N. Ozaki, Y. Hironaka, *et al.*, "Prediction of the superimposed laser shot number for copper using a deep convolutional neural network," Opt. Express **31**(15), 24045–24053 (2023).
17. B. Mills and J. A. Grant-Jacob, "Lasers that learn: The interface of laser machining and machine learning," IET Optoelectron. **15**(5), 207–224 (2021).

Optical Materials EXPRESS

18. A. N. Bakhtiyari, Z. Wang, L. Wang, *et al.*, "A review on applications of artificial intelligence in modeling and optimization of laser beam machining," Opt. Laser Technol. **135**, 106721 (2021).
19. J. A. Grant-Jacob, B. Mills, and R. W. Eason, "Parametric study of the rapid fabrication of glass nanofoam via femtosecond laser irradiation," J. Phys. D: Appl. Phys. **47**(5), 055105 (2014).
20. A. F. Courtier, J. A. Grant-Jacob, R. Ismaeel, *et al.*, "Laser-based fabrication of nanofoam inside a hollow capillary," Mater. Sci. Appl. **08**(12), 829–837 (2017).
21. A. V. Rode, E. G. Gamaly, and B. Luther-Davies, "Formation of cluster-assembled carbon nano-foam by high-repetition-rate laser ablation," Appl. Phys. A **70**(2), 135–144 (2000).
22. A. V. Rode, R. Elliman, E. G. Gamaly, *et al.*, "Electronic and magnetic properties of carbon nanofoam produced by high-repetition-rate laser ablation," Appl. Surf. Sci. **197-198**, 644–649 (2002).
23. K. Venkatakrishnan, D. Vipparty, and B. Tan, "Nanofibre fabrication by femtosecond laser ablation of silica glass," Opt. Express **19**(17), 15770–15776 (2011).
24. A. E. Fischer, K. A. Pettigrew, D. R. Rolison, *et al.*, "Incorporation of homogeneous, nanoscale MnO2 within ultraporous carbon structures via self-limiting electroless deposition: implications for electrochemical capacitors," Nano Lett. **7**(2), 281–286 (2007).
25. J. Guo and C. Wang, "A polymer scaffold binder structure for high capacity silicon anode of lithium-ion battery," Chem. Commun. **46**(9), 1428–1430 (2010).
26. Y. Nakayama, P. J. Pauzauskie, A. Radenovic, *et al.*, "Tunable nanowire nonlinear optical probe," Nature **447**(7148), 1098–1101 (2007).
27. P. Viswanathan, S. Chirasatitsin, K. Ngamkham, *et al.*, "Cell instructive microporous scaffolds through interface engineering," J. Am. Chem. Soc. **134**(49), 20103–20109 (2012).
28. P. Isola, J.-Y. Zhu, T. Zhou, *et al.*, "Image-to-image translation with conditional adversarial networks," in *Proceedings of the IEEE conference on computer vision and pattern recognition*, (2017), 1125–1134.
29. J. A. Grant-Jacob, B. Mills, and M. N. Zervas, "Visualizing laser ablation using plasma imaging and deep learning," Opt. Continuum **2**(7), 1678–1687 (2023).
30. University of Southampton, 2023, https://doi.org/10.5258/SOTON/D2738.